Open Quantum System Simulation of Faraday's Induction Law via Dynamical Instabilities

Elvia Colella[*], Arkadiusz Kosior, Farokh Mivehvar, and Helmut Ritsch

Institut für Theoretische Physik, Universität Innsbruck, A-6020 Innsbruck, Austria

We propose a novel type of a Bose-Hubbard ladder model based on an open quantum-gas–cavity-QED setup to study the physics of dynamical gauge potentials. Atomic tunneling along opposite directions in the two legs of the ladder is mediated by photon scattering from transverse pump lasers to two distinct cavity modes. The resulting interplay between cavity photon dissipation and the optomechanical atomic backaction then induces an average-density-dependent dynamical gauge field. The dissipation-stabilized steady-state atomic motion along the legs of the ladder leads either to a pure chiral current, screening the induced dynamical magnetic field as in the Meissner effect, or generates simultaneously chiral and particle currents. For a sufficiently strong pump the system enters into a dynamically unstable regime exhibiting limit-cycle and period-doubled oscillations. Intriguingly, an electromotive force is induced in this dynamical regime as expected from an interpretation based on Faraday's law of induction for the time-dependent synthetic magnetic flux.

Introduction.—Gauge theories describe a plethora of fundamental phenomena, from electromagnetism to the interaction between elementary particles [1]. Exploring limits of such theories has driven the interest toward the experimental implementation of "synthetic" gauge potentials in ultracold neutral atoms [2]. Early experiment successfully realized *static* background artificial gauge potentials [3–9]; however, in a genuine gauge theory the gauge potentials appear as *dynamical* degrees of freedom. In this respect, introducing a density dependence on the synthetic vector potential via the periodical modulation of two-body interactions [10,11] and Floquet lattice shaking [12,13] constitutes an important step towards implementing dynamical gauge potentials [14].

Among alternative approaches to induce dynamical gauge potentials, quantum-gas–cavity-QED setups stand out owing to the intrinsic dynamical nature of cavity fields [15,16]. Many interesting phenomena have been predicted to arise in systems with cavity-induced dynamical gauge potential, from the dynamical appearance of a vector potential at the onset of superradiance [17,18] to a dissipation-induced dynamical Peierls phase [19] and the Meissner-like expulsion of a magnetic field [20]. The prediction of cavity-induced dynamic spin-orbit coupling [21–28] and its recent realization [29] has opened a new avenue for engineering dynamical gauge potentials alongside free-space schemes and experiments [30].

Motivated by the recent experimental realization of the dynamical spin-orbit coupling [29] and a two-mode Dicke model [31], we propose a novel cavity-QED scheme for implementing an *average-density-dependent* dynamical

gauge potential. In particular, we develop a ladder model [32] with cavity-assisted counterpropagating tunnelings as shown in Fig. 1. A dynamic gauge potential appears at the onset of the superradiant photon scattering from two transverse pump lasers into two cavity modes owing to dissipation-induced phase shifts of cavity photons. In contrast to previous works [17–19], we take into account the optomechanical backaction of the atomic dynamics,
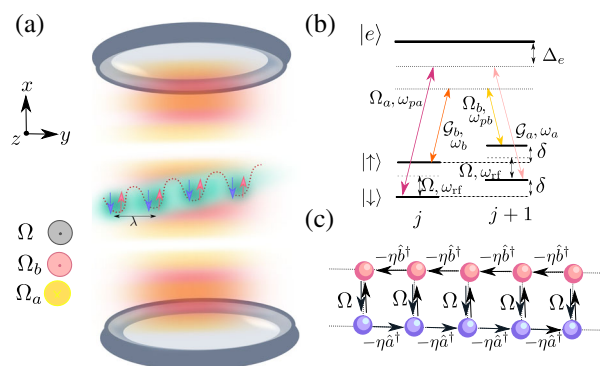

FIG. 1. Sketch of the setup. (a) A spinor BEC is loaded into a 1D tilted optical lattice perpendicular to the axis of a linear cavity. Neighboring sites are Raman coupled via two cavity modes with strengths $\mathcal{G}_{a,b}$ and transversely applied laser fields with amplitudes $\Omega_{a,b}$. A microwave couples the two atomic states locally with strength Ω. (b) Sketch of the atomic level structure and of the two independent two-photon Raman transitions inducing directional tunneling between neighboring lattice sites. (c) Effective mapping of the spinor BEC in the 1D lattice in panel (a) into a two-leg Bose-Hubbard ladder with cavity-assisted longitudinal hoppings and microwave-generated transverse tunneling.

leading to an average-density-dependent dynamical magnetic flux when the optomechanical backaction shifts significantly the cavity resonances and consequently the dissipation-induced photonic phases. The system exhibits three steady states: photon-balanced Meissner (PB-M) and vortex (PB-V) states and a photon-imbalanced biased ladder (PI-BL) phase. In addition, the phase diagram of the system features a region of highly nonlinear dynamics with no steady state. Two stable dynamical phases are identified with limit-cycle and period-doubled oscillations. Remarkably, an electromotive force is induced naturally in this regime, mimicking Faraday's law of induction.

Model.—Consider a spinor Bose-Einstein condensate (BEC) inside a linear optical cavity. The BEC is strongly confined by an external optical lattice to a one dimension perpendicular to the cavity axis at antinodes of two distinct cavity electromagnetic modes, $\hat{a}$ and $\hat{b}$; see Fig. 1(a). The natural tunneling of atoms along the lattice is suppressed by applying a potential gradient δ [33]. A directional hopping is restored by two independent resonant two-photon Raman transitions as shown in Fig. 1(b): The ground pseudospin state $|\downarrow\rangle$ ($|\uparrow\rangle$) is coupled, respectively, by Rabi rates $\mathcal{G}_a$ ($\mathcal{G}_b$) and Ω_a (Ω_b) to a far detuned excited state $|e\rangle$ via the cavity mode $\hat{a}$ ($\hat{b}$) with resonance frequency ω_a (ω_b) and an out-of-plane transverse pump laser with frequency ω_{pa} (ω_{pb}). The two pseudospin ground states are coupled on site with a rate Ω through a radio-frequency drive with frequency $\omega_{\rm rf}$.

For large atomic detuning, the excited state can be adiabatically eliminated. By only retaining resonant scattering terms, the effective Hamiltonian reads [34],

$$
\begin{aligned}
\hat{H} = &-\hbar\eta \sum_{j=1}^{L}(\hat{a}^\dagger \hat{c}^\dagger_{\downarrow,j+1}\hat{c}_{\downarrow,j} + \hat{b}\hat{c}^\dagger_{\uparrow,j+1}\hat{c}_{\uparrow,j} + \text{H.c.}) \\
&-\hbar\Omega \sum_{j=1}^{L}(\hat{c}^\dagger_{\uparrow,j}\hat{c}_{\downarrow,j} + \text{H.c.}) \\
&+\frac{V}{2}\sum_{j=1}^{L}\sum_{\sigma=\uparrow,\downarrow}\hat{N}_{\sigma,j}(\hat{N}_{\sigma,j}-1) + \gamma V \sum_{j=1}^{L}\hat{N}_{\downarrow,j}\hat{N}_{\uparrow,j} \\
&-\hbar(\Delta_a - U\hat{N}_\downarrow)\hat{a}^\dagger\hat{a} - \hbar(\Delta_b - U\hat{N}_\uparrow)\hat{b}^\dagger\hat{b}, \quad (1)
\end{aligned}
$$

where $\hat{c}_{\sigma,j}$ is the atomic bosonic annihilation operator for pseudospin σ at site j, and $\hat{N}_\sigma = \sum_j \hat{N}_{\sigma,j} = \sum_j \hat{c}^\dagger_{\sigma,j}\hat{c}_{\sigma,j}$. The effective model (1) constitutes a spinor Bose-Hubbard-type Hamiltonian with cavity-induced dynamical spin-orbit coupling. It can be effectively mapped into a two-leg Bose-Hubbard ladder of length L, with one of the two pseudospin states acting as a synthetic dimension [35]. In this spirit, the first row of the Hamiltonian corresponds to the motion of the atoms along the longitudinal direction (i.e., legs) of the ladder. The forward tunneling amplitudes, $\hat{t}_{a(b)} \equiv \hbar\eta\hat{a}^\dagger(\hat{b})$, are restored by scattering photons from the pump (cavity)

into the cavity (pump) at a rate $\eta = \mathcal{G}_a\Omega_a/\Delta_e = \mathcal{G}_b\Omega_b/\Delta_e$, with $\Delta_e = \omega_p - \omega_e$ being the effective atomic detuning from the average pump frequency $\omega_p = (\omega_{pa} + \omega_{pb})/2$. The second line represents a transversal hopping along rungs of the ladder, with tunneling amplitude set by the radio-frequency coupling Ω. The third line includes repulsive two-body on-site atomic interactions, with V being the strength of intraspecies interactions and γ parametrizing the ratio between the strength of inter- and intraspecies interactions. The last two terms represent the free energy of the photon fields with the cavity detunings defined as $\Delta_{a(b)} = \omega_p \pm \omega_{\rm rf}/2 - \omega_{a(b)}$, where in the following we assume $\Delta \equiv \Delta_a = \Delta_b$. The cavity resonances are shifted by the atomic medium $U\hat{N}_\sigma$, where $U = \mathcal{G}_a^2/\Delta_e = \mathcal{G}_b^2/\Delta_e$ is the dispersive shift per atom.

Average-density-dependent dynamical gauge potential and synthetic magnetic field.—Let us now describe the mechanism by which a dynamical gauge potential can arise when the photon-assisted tunnelings $\hat{t}_{a,b}$ are restored. We recall that on a lattice, the coupling of a charged particle $\mathcal{Q}$ to a vector potential $\mathcal{A}$ is manifested by the phase factor $e^{i\mathcal{Q}/\hbar \int_{\rm path} \mathcal{A}\cdot d\mathbf{l}}$ of the tunneling amplitude, i.e., Peierls phase [36]. The Peierls phase is fixed by the circulation of the vector potential along the path enclosing the unit cell, and reduces to the Aharonov-Bohm phase in the continuum limit [37]. Therefore, the magnetic flux piercing a lattice plaquette is $\Phi_B = \int_{\rm unit\ cell} \mathcal{A}\cdot d\mathbf{l}$.

For neutral atoms the vector potential must be engineered tailoring the atomic tunneling amplitudes. To achieve this, our scheme exploits the superradiant scattering of photons into the cavity. In particular, in the superradiant phase the collective synchronized emission of photons results in a macroscopic occupation of the two cavity modes, which can be treated semiclassically as dynamical electromagnetic fields. The cavity fields are thus described by coherent states [38], $\hat{a} \to \langle\hat{a}\rangle \equiv \alpha = |\alpha|e^{i\phi_\alpha}$ and $\hat{b} \to \langle\hat{b}\rangle \equiv \beta = |\beta|e^{i\phi_\beta}$, and the tunneling amplitudes for the lower and upper leg, respectively, reduce to c numbers $t_a = \hbar\eta|\alpha|e^{i\phi_\alpha}$ and $t_b = \hbar\eta|\beta|e^{-i\phi_\beta}$. The pumping geometry is equivalent to a well-defined gauge choice where the transverse component of the vector potential along the rungs $\mathcal{A}_j^\perp = 0$ vanishes, and its longitudinal components depend on the phases of the cavity fields $\mathcal{A}_{a,j}^\parallel \propto \phi_\alpha$ and $\mathcal{A}_{b,j}^\parallel \propto -\phi_\beta$. Hence, the total phase acquired by the atomic wave function around a closed loop along one plaquette is $\Phi = \phi_\alpha + \phi_\beta$. The dynamics of the atoms is equivalent to the one of charge particles $\mathcal{Q}$ threaded by the magnetic flux $\Phi_B = \hbar\Phi/\mathcal{Q} = \Phi_{0B}\Phi/2\pi$ with $\Phi_{0B} = h/\mathcal{Q}$.

In the adiabatic limit for the photonic dynamics [15,16], the cavity fields can be slaved to the atomic degrees of freedom and be obtained from the stationary solution of the Heisenberg equations of motion, $\alpha = -\eta\Theta_\downarrow/(\Delta_a - U N_\downarrow + i\kappa_a)$ and $\beta = -\eta\Theta_\uparrow^*/(\Delta_b - U N_\uparrow + i\kappa_b)$, where $\kappa_{a,b}$ are the

decay rates of the cavity fields and $N_\sigma = \langle \hat{N}_\sigma \rangle$. This prescribes the phase locking between the photons and the average atomic hopping operators, $\Theta_\sigma = \sum_j \langle c^\dagger_{\sigma,j+1} c_{\sigma,j} \rangle$. Up to a global phase, the phases of the cavity fields are uniquely determined [34],

$$\phi_{\alpha(\beta)} = -\arctan\left(\frac{\kappa_{a(b)}}{\Delta_{a(b)} - U N_{\downarrow(\uparrow)}}\right). \quad (2)$$

The atomic ladder acts as a refractive medium for the light inside the resonator dispersively shifting the cavity resonances, i.e., $\Delta_{a(b)} - U N_{\downarrow(\uparrow)}$, and the magnetic flux $\Phi_B \propto \phi_\alpha + \phi_\beta$ becomes nonlinearly dependent on the atomic leg density.

In order to unveil the effect of the cavity-induced magnetic field, let us consider the single-particle physics. The atomic part of the Hamiltonian (1) can be diagonalized to yield the single-particle atomic energy bands,

$$\frac{\epsilon_\pm(q)}{\hbar} = -\eta F_+ + \frac{U}{2} n_{\mathrm{ph}} \pm \sqrt{\Omega^2 + \left(\eta F_- - \frac{U}{2}\Delta n_{\mathrm{ph}}\right)^2}. \quad (3)$$

Here we have defined $F_\pm(q) = |\alpha|\cos(q + \phi_\alpha) \pm |\beta|\cos(q - \phi_\beta)$, $n_{\mathrm{ph}} = n_\alpha + n_\beta = |\alpha|^2 + |\beta|^2$ as the total number of photons, and $\Delta n_{\mathrm{ph}} = n_\alpha - n_\beta$ as the photon-number difference. The quasimomentum q is minimally coupled to the photon phases $\phi_{\alpha,\beta}$, and is conserved during the dynamics for the noninteracting system. The self-consistent band structure exhibits different behaviors depending on Δn_{ph}. For the photon-balanced (PB) case, $\Delta n_{\mathrm{ph}} = 0$, the lowest energy band has either a single minimum at $q = 0$ or symmetric double minima at $q = \pm q_m \neq 0$. The atomic ground state corresponds to a Meissner (M) and a vortex (V) phase, respectively. For the photon-imbalanced (PI) case, $\Delta n_{\mathrm{ph}} \neq 0$, the energy bands become asymmetric, with the lowest band developing a single minimum at a nonzero quasimomentum, $q = q_m \neq 0$. The photon imbalance drives an atomic population imbalance in the two legs, which breaks the $\mathbb{Z}_2$ reflection symmetry of the system corresponding to the invariance under the exchange of the cavity modes $\hat{a} \leftrightarrow \hat{b}^\dagger$ and ladder legs $\hat{c}_{\uparrow,j} \leftrightarrow \hat{c}_{\downarrow,j}$. We identify this state as the biased ladder (BL) phase [39–41].

We find the steady state of the system by looking at the long-time dynamics of the coupled Heisenberg equations of motion with periodic boundary conditions, starting from a uniform density distribution with zero quasimomentum [34]. The steady-state phase diagram in the Δ–η parameter plane is mapped out in Fig. 2(a) for $N = 1$. Typical self-consistent energy bands are presented in Fig. 2(b). In this noninteracting low-density regime $\bar{n} = \bar{n}_\downarrow + \bar{n}_\uparrow = 1/2L \ll 1$, the optomechanical backaction $U N_\sigma$ of the
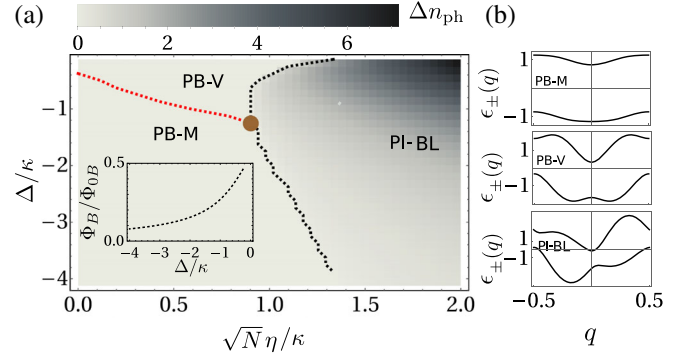

FIG. 2. Single-particle phase diagram. (a) The steady-state phase diagram in the $\{\sqrt{N}\eta/\kappa, \Delta/\kappa\}$ parameter plane. The self-consistent band structure exhibits three distinct phases: PB-M and PB-V, and PI-BL states. The color map indicates the photon imbalance Δn_{ph}. The red dashed curve separating the PB-M and the PB-V states has been obtained analytically [34]. The three phases intersect in a tricritical point indicated by the brown dot. Inset: The synthetic magnetic flux Φ_B/Φ_{0B} as a function of Δ/κ. For $\Delta/\kappa = -0.5$, (b) typical band structure $\epsilon_\pm(q)$ in each phase corresponding to $\sqrt{N}\eta/\kappa = \{0.08, 0.50, 1.00\}$. Other parameters are set to $L = 51$, $U = \Delta/2L$, $\Omega = 1$, and $V = \gamma = 0$.

atomic medium on the cavity resonances is negligible. Therefore, the magnetic flux Φ_B is almost density independent and can only be tuned by varying the cavity parameters Δ and κ; see the inset of Fig. 2(a).

By increasing the ladder density $\bar{n} = N/2L$, the dispersive shift $U N_\sigma$ becomes significant, and the density dependence of the induced magnetic flux Φ_B becomes apparent. Figure 3(a) shows for weak on-site interactions the stationary value of the magnetic flux Φ_B/Φ_{0B} as a function of the average atomic density $\bar{n} = N/2L$ and the pump strength $\sqrt{N}\eta$ for cavity detuning, $\Delta = -6\kappa$. The gray color indicates a dynamical region with no steady-state solution. Figure 3(a) shows that density effects become relevant for higher fillings, where the two cavity modes are dispersively shifted closer to resonance. The total photon number n_{ph} and the relative photon number difference $|\Delta n_{\mathrm{ph}}|/n_{\mathrm{ph}}$ are shown in Figs. 3(b) and 3(c), respectively. The system exhibits a phase transition from a photon balanced to a photon imbalanced phase when the pumping strength is increased (white solid line in Fig. 3). For large cavity detunings the weak magnetic fields, $\Phi_B/\Phi_{0B} < 0.15$, do not support a PB-V phase transition at weak pumping.

Superradiance and persistent currents.—Since each photon scattering process is accompanied by a directional atomic tunneling along the legs of the ladder, stationary currents flowing in opposite directions are generated in the superradiant phase; see the sketch in Fig. 1(c). Dissipation plays an essential role in the generation of these currents [19]. By inspection of the leg currents,
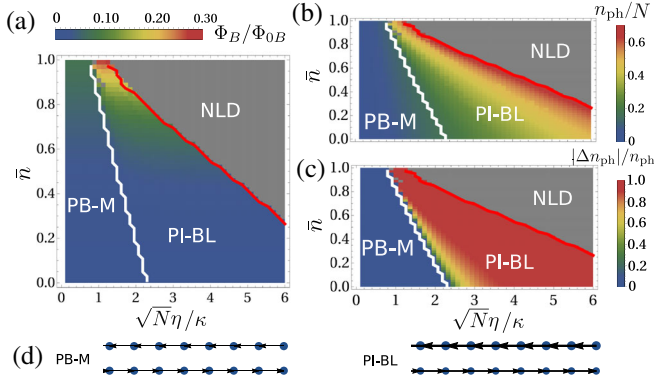
FIG. 3. Many-body phase diagram. (a) Nonequilibrium phase diagram in the $\{\sqrt{N}\eta/\kappa, \bar{n}\}$ parameter plane. For $\Delta/\kappa = -6$, the system exhibits only two of the steady-state phases of Fig. 2(a): the PB-M and the PI-BL states. The two phases are separated by the solid white line. The gray area indicates a region of dynamical instability with no steady state. The color map indicates the steady-state synthetic magnetic flux Φ_B, clearly showing average-density dependence. The total photon number n_{ph} (b) and the photon number difference $\Delta n_{\mathrm{ph}}/n_{\mathrm{ph}}$ (c) are shown in the same parameter plane. Photon number saturates the scale in the bright blue region in (b). (d) Current patterns in the PB-M and the PI-BL states. Parameters are the same as Fig. 2, except $VN = 1$, $\gamma = 0.1$.

$J_{\downarrow} = i\eta \sum_j \langle a^{\dagger} \hat{c}_{\downarrow,j+1}^{\dagger} \hat{c}_{\downarrow,j} - \mathrm{H.c.}\rangle$ and $J_{\uparrow} = i\eta \sum_j \langle \hat{b} \hat{c}_{\uparrow,j+1}^{\dagger} \hat{c}_{\uparrow,j} - \mathrm{H.c.}\rangle$, one sees that for the steady state the leg currents are proportional to the photon number of the respective coupled modes, $J_{\downarrow} = 2\kappa|\alpha|^2$ and $J_{\uparrow} = -2\kappa|\beta|^2$. The chiral current is determined by the total number of photons leaked out of the cavity, $J_c = J_{\downarrow} - J_{\uparrow} = 2\kappa n_{\mathrm{ph}}$, while the photon number difference identifies the net particle current, $J_p = J_{\downarrow} + J_{\uparrow} = 2\kappa \Delta n_{\mathrm{ph}}$. The current patterns are illustrated schematically in Fig. 3(d). At weak pumpings, a Meissner phase is stabilized with a pair of equal, counter-propagating currents flowing along the two legs. At stronger pump strengths a net particle current is driven by the photon imbalance in the biased ladder phase [39–41].

Dynamical instabilities and Faraday's induction law.— We now take a closer look into the gray region of Fig. 3, where the system exhibits a highly nonlinear dynamics (NLD). When the long-time dynamics is characterized by periodic oscillation of the cavity field amplitudes [see Figs. 4(a) III and 4(b) III], the system behaves like a limit-cycle oscillator. Self-sustained periodic oscillations of the cavity modes spontaneously emerge in the absence of an external periodic drive, breaking the time-translational symmetry [42]. The time-translational symmetry breaking in driven-dissipative systems has been recently interpreted as a dissipative time crystal [43,44]. The system also exhibits a period-doubling bifurcation at stronger pumping with the appearance of an additional halved frequency
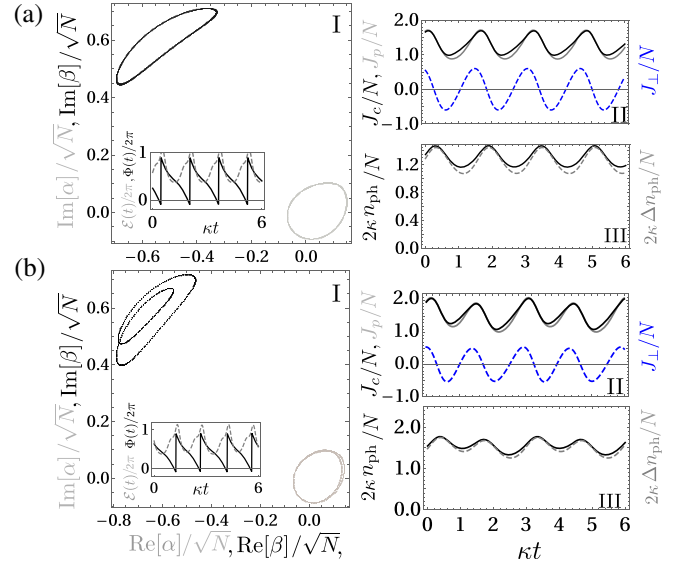

FIG. 4. Periodic nonlinear dynamics for high densities $\bar{n} = 1.42$. The phase space trajectories of the two cavity-mode amplitudes α (gray) and β (black) for long-time dynamics with $\sqrt{N}\eta/\kappa = 1.3$ (a) and 1.55 (b) [outside of the phase diagram of Fig. 3]. Insets in panels (I): Time evolution of the magnetic flux (black) and e.m.f (dashed gray). Time evolution of the induced chiral J_c (black), particle J_p (dashed gray), and rung $J_{\perp}$ (dotted blue) currents (II), and of the total photon number n_{ph} (black) and the photon number difference Δn_{ph} (dashed gray) (III). Panel (a) exhibits stable limit-cycle oscillations, while panel (b) shows period-doubled oscillations. Other parameters are the same as Fig. 3 for $N = 140$.

component above the main limit-cycle oscillation frequency, possibly leading to chaos [45].

The nontrivial dynamics of the photonic phases shown in Fig. 4 leads to a time-dependent magnetic flux $\Phi_B(t)$. This in turn induces an electromotive force $\mathcal{E}(t) = -\partial\Phi_B(t)/\partial t = -(\Phi_{0B}/2\pi)\partial\Phi(t)/\partial t$, with

$$\frac{\partial\Phi(t)}{\partial t} = 2\Delta - UN - \frac{K_{\downarrow}}{2|\alpha|^2} - \frac{K_{\uparrow}}{2|\beta|^2}, \qquad (4)$$

and the average longitudinal kinetic energies, $K_{\downarrow} = -2\eta\mathrm{Re}(\alpha^*\Theta_{\downarrow})$ and $K_{\uparrow} = -2\eta\mathrm{Re}(\beta^*\Theta_{\uparrow}^*)$. The time evolution of the magnetic flux and the induced electromotive force are shown in the insets of Figs. 4(a) I and 4(b) I. The time-dependent electromotive force drives periodically the atomic population between the two legs, apparent from the oscillating chiral J_c, particle J_p, and the emerging rung current $J_{\perp} = i\Omega \sum_j \langle \hat{c}_{\uparrow,j}^{\dagger} \hat{c}_{\downarrow,j} - \mathrm{H.c.}\rangle$; see Figs. 4(a) II and 4(b) II. In contrast to the steady-state results the photon-number counts are no longer an exact measurement of the leg currents. One can think of the residual currents as induction currents which oppose the variation of the magnetic flux, thus mimicking Faraday's law of induction with neutral particles [46].

Experimental considerations.—Our proposal can be realized by driving two optical transitions of ^{87}Rb atoms as in Ref. [29]. Several atomic ladders can be experimentally isolated from single rows of a 2D optical lattice in the plane intercepted by the cavity axis and the y direction. The size of the ladder in the y direction is strictly limited by the cavity waist w_0. Assuming a transversal size of $2w_0 \sim 150 \; \mu m$, an atomic cloud of $\ell_y \sim 70 \; \mu m$, and an optical lattice with the lattice constant $a = \lambda_{851 \; nm}/2 = 0.426 \; \mu m$, the ladder would have $N_{u.c} = \ell_y/a \sim 160$ unit cells. Upon redistribution of the cloud into the 2D lattice, and assuming a longitudinal cloud size of $\ell_x \sim 2\ell_y$, the filling of the 2D lattice can be varied in a range of $\nu = N/(\ell_x \ell_y) \in [0.1, 2]$ for an atomic cloud of $N \sim 0.05$–1.1×10^5 atoms, respectively. The impact of the dispersive shifts UN_σ on the cavity resonances is significant in the strong light-matter coupling limit. A good measure of the coupling strength is provided by the parameter UN/κ, expressing the ratio between the coherent and incoherent processes in the system. For a high-finesse cavity with a linewidth of $2\kappa = 17$ kHz, $U = 91$ kHz as in Ref. [47], and $N = 4 \times 10^5$ atoms, the optomechanical backaction, $UN/\kappa \sim 2.5 > 1$, is in a desired range to observe the predicted phenomena. Our scheme allows us to nondestructively measure the phase diagram by monitoring photons leaking out of the cavity [15]. The steady-state atomic currents can be obtained from the population count of the two cavity modes at the detector. The magnetic flux can be inferred through homodyne detection by measuring the phase of the two mode with respect to a probe laser.

Conclusions.—We studied the emergence of an average-density-dependent dynamical U(1) gauge potential when the motion of neutral atoms is strongly coupled to two high-Q cavity modes. The gauge potential stems from the delicate interplay between the optomechanical atomic backaction on the cavity fields and photon dissipation into the environment. It differs from previously studied cavity-induced gauge potentials which do not feature any atomic-density dependence [17–19,21–27,27–29,48]. Emerging dynamical instabilities with stable limit-cycle and period-doubled oscillations can be interpreted as driven by an effective oscillating electromotive force according to Faraday's law of induction. Our proposed scheme offers a unique possibility to explore these exotic nonequilibrium phenomena in state-of-the-art quantum-gas–cavity-QED experiments.

[*]elvia.colella@uibk.ac.at

[1] U.-J. Wiese, Ann. Phys. (Amsterdam) **525**, 777 (2013).
[2] J. Dalibard, F. Gerbier, G. Juzeliūnas, and P. Öhberg, Rev. Mod. Phys. **83**, 1523 (2011).
[3] P. Engels, I. Coddington, P. C. Haljan, V. Schweikhard, and E. A. Cornell, Phys. Rev. Lett. **90**, 170405 (2003).
[4] Y.-J. Lin, R. L. Compton, K. Jiménez-García, J. V. Porto, and I. B. Spielman, Nature (London) **462**, 628 (2009).
[5] Y. J. Lin, K. Jiménez-García, and I. B. Spielman, Nature (London) **471**, 83 (2011).
[6] M. Aidelsburger, M. Atala, S. Nascimbène, S. Trotzky, Y.-A. Chen, and I. Bloch, Phys. Rev. Lett. **107**, 255301 (2011).
[7] J. Struck, C. Ölschläger, M. Weinberg, P. Hauke, J. Simonet, A. Eckardt, M. Lewenstein, K. Sengstock, and P. Windpassinger, Phys. Rev. Lett. **108**, 225304 (2012).
[8] M. Aidelsburger, M. Atala, M. Lohse, J. T. Barreiro, B. Paredes, and I. Bloch, Phys. Rev. Lett. **111**, 185301 (2013).
[9] M. Aidelsburger, M. Lohse, C. Schweizer, M. Atala, J. T. Barreiro, S. Nascimbène, N. R. Cooper, I. Bloch, and N. Goldman, Nat. Phys. **11**, 162 (2015).
[10] S. Greschner, G. Sun, D. Poletti, and L. Santos, Phys. Rev. Lett. **113**, 215303 (2014).
[11] L. W. Clark, B. M. Anderson, L. Feng, A. Gaj, K. Levin, and C. Chin, Phys. Rev. Lett. **121**, 030402 (2018).
[12] A. P. Itin and M. I. Katsnelson, Phys. Rev. Lett. **115**, 075301 (2015).
[13] F. Görg, K. Sandholzer, J. Minguzzi, R. Desbuquois, M. Messer, and T. Esslinger, Nat. Phys. **15**, 1161 (2019).
[14] N. Goldman, G. Juzeliūnas, P. Öhberg, and I. B. Spielman, Rep. Prog. Phys. **77**, 126401 (2014).
[15] H. Ritsch, P. Domokos, F. Brennecke, and T. Esslinger, Rev. Mod. Phys. **85**, 553 (2013).
[16] F. Mivehvar, F. Piazza, T. Donner, and H. Ritsch, Adv. Phys. **70**, 1 (2021).
[17] C. Kollath, A. Sheikhan, S. Wolff, and F. Brennecke, Phys. Rev. Lett. **116**, 060401 (2016).
[18] E. Colella, F. Mivehvar, F. Piazza, and H. Ritsch, Phys. Rev. B **100**, 224306 (2019).
[19] W. Zheng and N. R. Cooper, Phys. Rev. Lett. **117**, 175302 (2016).
[20] K. E. Ballantine, B. L. Lev, and J. Keeling, Phys. Rev. Lett. **118**, 045302 (2017).
[21] F. Mivehvar and D. L. Feder, Phys. Rev. A **89**, 013803 (2014).
[22] L. Dong, L. Zhou, B. Wu, B. Ramachandhran, and H. Pu, Phys. Rev. A **89**, 011602(R) (2014).
[23] Y. Deng, J. Cheng, H. Jing, and S. Yi, Phys. Rev. Lett. **112**, 143007 (2014).
[24] F. Mivehvar and D. L. Feder, Phys. Rev. A **92**, 023611 (2015).
[25] S. Ostermann, H.-W. Lau, H. Ritsch, and F. Mivehvar, New J. Phys. **21**, 013029 (2019).
[26] F. Mivehvar, H. Ritsch, and F. Piazza, Phys. Rev. Lett. **122**, 113603 (2019).
[27] C.-M. Halati, A. Sheikhan, and C. Kollath, Phys. Rev. A **99**, 033604 (2019).
[28] S. Ostermann, H. Ritsch, and F. Mivehvar, Phys. Rev. A **103**, 023302 (2021).

[29] R. M. Kroeze, Y. Guo, and B. L. Lev, Phys. Rev. Lett. **123,** 160404 (2019).

[30] V. Lienhard, P. Scholl, S. Weber, D. Barredo, S. de Léséleuc, R. Bai, N. Lang, M. Fleischhauer, H. P. Büchler, T. Lahaye, and A. Browaeys, Phys. Rev. X **10,** 021031 (2020).

[31] A. Morales, D. Dreon, X. Li, A. Baumgärtner, P. Zupancic, T. Donner, and T. Esslinger, Phys. Rev. A **100,** 013816 (2019).

[32] E. Orignac and T. Giamarchi, Phys. Rev. B **64,** 144515 (2001).

[33] D. Jaksch and P. Zoller, New J. Phys. **5,** 56 (2003).

[34] See Supplemental Material at http://link.aps.org/supplemental/10.1103/PhysRevLett.128.070603 for further details.

[35] A. Celi, P. Massignan, J. Ruseckas, N. Goldman, I. B. Spielman, G. Juzeliūnas, and M. Lewenstein, Phys. Rev. Lett. **112,** 043001 (2014).

[36] R. Peierls, Z. Phys. **80,** 763 (1933).

[37] Y. Aharonov and D. Bohm, Phys. Rev. **115,** 485 (1959).

[38] F. Piazza, P. Strack, and W. Zwerger, Ann. Phys. (Amsterdam) **339,** 135 (2013).

[39] R. Wei and E. J. Mueller, Phys. Rev. A **89,** 063617 (2014).

[40] S. Uchino and A. Tokuno, Phys. Rev. A **92,** 013625 (2015).

[41] S. Greschner, M. Piraud, F. Heidrich-Meisner, I. P. McCulloch, U. Schollwöck, and T. Vekua, Phys. Rev. A **94,** 063628 (2016).

[42] K. Sacha and J. Zakrzewski, Rep. Prog. Phys. **81,** 016401 (2018).

[43] H. Keßler, J. G. Cosme, M. Hemmerling, L. Mathey, and A. Hemmerich, Phys. Rev. A **99,** 053605 (2019).

[44] H. Keßler, P. Kongkhambut, C. Georges, L. Mathey, J. G. Cosme, and A. Hemmerich, Phys. Rev. Lett. **127,** 043602 (2021).

[45] F. Piazza and H. Ritsch, Phys. Rev. Lett. **115,** 163601 (2015).

[46] J. Maxwell, *A Treatise on Electricity and Magnetism* (Dover Publications, New York, 1954).

[47] T. Elsässer, B. Nagorny, and A. Hemmerich, Phys. Rev. A **69,** 033403 (2004).

[48] C.-M. Halati, A. Sheikhan, and C. Kollath, Phys. Rev. A **96,** 063621 (2017).